ACS APPLIED MATERIALS & INTERFACES

RESEARCH ARTICLE

www.acsami.org

In situ Evolution of Trivalent Chromium Process Passive Film on Al in a Corrosive Aqueous Environment

Xuecheng Dong, Sandip Argekar, Peng Wang, and Dale W. Schaefer*

School of Energy, Environment, Biological and Medical Engineering, University of Cincinnati, Cincinnati, Ohio 45221-0012, United States

ABSTRACT: In situ neutron reflectivity (NR) is used to observe the structure and evolution of a Trivalent Chromium Process (TCP) passive film on Al in a NaCl-D_2O solution. Using a split liquid reflectivity cell we mimicked the corrosion process on the anodic sites in alloy AA 2024-T3 in a pitting scenario. The split cell separates the anodic and cathodic reactions, allowing NR observation of the corroding anodic surface under potential control. We observed the evolution of the TCP film on the Al anode and compared the degradation of the Al with and without TCP protection. When held at 100 mV above the open-circuit potential (OCP), unprotected aluminum dissolves at a rate of 120 Å/h. By contrast, TCP-coated Al is stable up to the pitting potential (200 mV above OCP). In the passive state D_2O molecules penetrate the bulk TCP film by partially replacing the hydrate water. In spite of exchange of hydration water, the TCP film is stable and the underlying aluminum is fully protected. The passive character of the TCP film is due to a dense layer at the metal-TCP interface and/or to suppression of ion transport in the bulk film. As the pitting potential is approached the film swells and NaCl-D_2O solution penetrates the TCP film. At this point, 50 vol % of the TCP film is occupied by bulk NaCl-D_2O solution. Failure occurs by aluminum dissolution under the swollen TCP film as the imbibed solution contacts the Al metal. Further increase in potential leads to complete stripping of the TCP film.

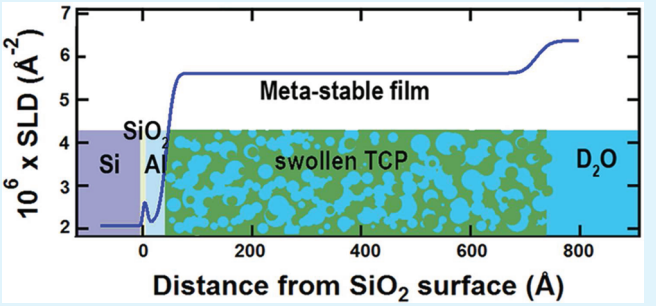

KEYWORDS: trivalent chromium process, TCP, passivation, Al, AA2024, neutron reflectivity, passive film

1. INTRODUCTION

AA 2024-T3 is a heat treatable aluminum alloy containing Cu and Mg. The alloy offers high strength-to-weight ratio so this alloy is widely used in the aircraft industry. AA 2024-T3, however, is susceptible to pitting corrosion in chloride-containing environments due to its high Cu content (3.8−4.9 wt %). Heterogeneous precipitation of Cu and other minor elements during heat treatment results in Cu-rich inclusions. As the native oxide layer on the alloy surface breaks down, preferential dissolution of light metals occurs from Cu-rich inclusions (for example, Al and Mg from Al_2CuMg).[1] The porous Cu remnants that result from this dealloying process act as cathodes on the alloy surface and promote further dissolution of surrounding Al matrix, hence the propagation of the pits.[1,2]

Pretreatments are used to mitigate pitting corrosion, chromate being particularly effective. For health concerns, however, chromate-based inhibitor systems are restricted in many nations. Alternative inhibitor systems with equal performance but less toxicity are the object of current research.[3−8] Extensive evaluation of nonchromate aluminum pretreatments by Environmental Security Technology Certification Program (ESTCP)[9,10] finds that among the potential chromate replacements, the NAVAIR trivalent chromium process (TCP) performs best on AA 2024-T3 alloy. Variants of TCP pretreatments based on the NAVAIR formulation have been commercialized by companies such as Henkel, Chemetall, and Surtech.

Recent research has clarified the TCP deposition mechanism.[11−13] The core components of the formulation include $Cr_2(SO_4)_3$, K_2ZrF_6, and HF.[14] Cr(III) and Zr(IV) form hydroxides near substrate surface where pH increases because of the cathodic proton reduction reaction. F^- ions in the TCP precursor solution promote activation of the aluminum alloy surface alloy surface. The native Al_2O_3 passive film dissolves as $[AlF_6]^{3-}$, exposing the bare metal. It is believed that the native aluminum oxide is stripped before TCP deposition proceeds.

The deposited TCP layer undoubtedly acts as physical barrier of some type that isolates the underlining metal from the aqueous environment. The interfacial morphology and its response to an active corrosion environment, however, are not known. Additionally pitting corrosion still compromises TCP-coated AA 2024-T3, which motivates our focus on anodically polarized surfaces, where pitting initiates.

We introduce an in situ method to quantify this uncharted area using neutron reflectivity (NR) in a potential-controlled split liquid cell. We address four questions: (1) does in situ NR data correlate with the electrochemical response; (2) what is the morphology of the TCP film in the potential range where the film is electrochemically passive; (3) what is the response of the passive

Received: June 29, 2011
Accepted: September 28, 2011
Published: September 28, 2011

TCP film as a function of potential in an corrosive environment; (4) how does the TCP film fail?

We investigated the electrochemical and morphological response of TCP film in a pitting scenario by combining electrochemistry and neutron reflectivity (NR). NR is a powerful tool for interface research. NR yields in situ chemical and structural information at the interface between the substrate and various environments including water.[15−17] Our approach, which combines electrochemistry and NR, employs a liquid-filled cell that holds two wafer electrodes (anode working electrode and cathode counter electrode) as well as a reference electrode used to monitor the potential of the working electrode. The cell allows us to track the evolution of the anode surface in an aqueous corrosion environment by NR. This approach circumvents the limitations of conventional electrochemical investigations, which are inevitably compromised by the intermetallic structure where anodes and cathodes are intermingled. The information derived from the split liquid reflectivity cell regarding the TCP response on a well-defined Al anode is unique in corrosion science.

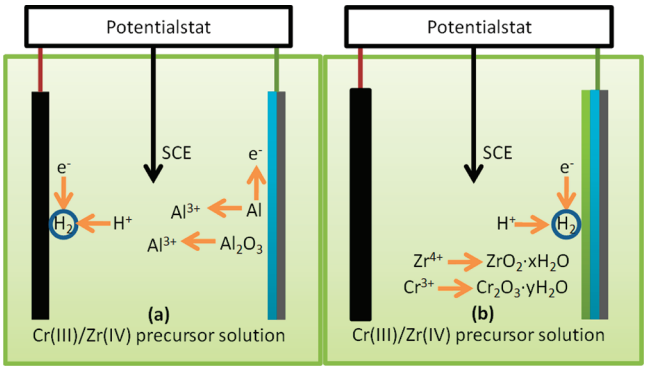

Figure 1. Schematic diagram of the TCP deposition on Al-coated wafers. (a) The substrate is anodically activated in a 10 vol % TCP bath. The native oxide and part of the Al dissolve. (b) Under cathodic polarization, proton reduction occurs on the Al surface. The pH rise triggers TCP deposition.

2. EXPERIMENTAL DETAILS

2.1. Silicon Wafer Substrates. Silicon wafers are readily available and ideally smooth for NR. The wafers are one-side-polished single crystal (111) (75 mm diameter, and 5 mm thickness) obtained from Wafer World, Inc. (West Palm Beach, FL. USA). A standard cleaning process (Piranha etching[18] followed by ethanol rinsing) was applied on each wafer. The Piranha etching solution contains H_2SO_4 (98%) from Pharmco-Aaper, Inc. (Brookfield, CT. USA) and H_2O_2 (30%) from Fisher Scientific, (Fair Lawn, NJ. USA). The two components were mixed in volume ratio of 3:1. Each wafer was etched at 90−100 °C for 3−5 min in the Piranha solution and rinsed with pure water followed by 200 proof absolute ethanol from Pharmco-Aaper, Inc. The wafers were rinsed until ethanol did not bead up on the wafer surface. Then the wafers were dried in N_2 and stored in sealed container prior the electron beam (e-beam) deposition of the aluminum coating.

The e-beam metal deposition on both anode and cathode wafers was performed in a vacuum deposition chamber at a pressure of 1×10^{-4} Torr. The material to be evaporated for forming a metal coating is in the form of an ingot. The thickness of metal coating is controlled by deposition time. The e-beam depositions were performed at Advanced Materials Characterization Center at the University of Cincinnati. The instrument is a FC1800 e-Beam Evaporator from Airco Temescal, USA. An Al ingot was used to prepare the Al-coated anode wafer. We used a pure Al coating to represent Al matrix anode in AA 2024-T3. The thickness of Al layer was controlled at 400−800 Å, which gives good smoothness and adequate thickness. We tested Cu and Au as noble-metal cathodes on Si wafers. The choice of Cu originated from AA 2024-T3 alloy composition. However the lifetime and degradation rate of Cu layer were not compatible with the requirements of the split liquid cell. We eventually settled on Au with a Cr buffer layer to enhance adhesion to the wafer substrate.

2.2. TCP Deposition. The TCP coating on Al-coated wafer substrates was deposited under cathodic polarization by an electro-assisted (EA) method.[15] The EA deposition was inspired by the generally accepted mechanism of TCP immersion deposition. In brief, TCP deposition is triggered by the thinning of the native oxide and resulting pH increase due to proton reduction at cathodic sites on an alloy surface.[19−24] EA deposition mimics both the oxide thinning and pH increase due to proton reduction reaction. In addition, the method guarantees a uniform potential distribution and controlled film growth all over the Al-coated wafer. Well-defined TCP films were demonstrated in previous work.[15] A potentiostat (Gamry PCI4 300) was used to control the EA process. The two-step EA deposition process was optimized as a brief anodic polarization (+0.50 V vs SCE, 30 s) to strip the native oxide (Figure 1a), followed by cathodic deposition for 3 min (Figure 1b). We investigated two different cathodic potentials (−1.50 V vs SCE, and −1.25 vs SCE) on AA 2024-T3 first, but eventually settled on −1.50 V as the standard for preparing Al-coated wafer substrates.

The TCP system studied is a simplified version of the original NAVAIR formulation.[14] The simplified formulation was chosen based on the film composition reported in our previous work.[15] In cathodic deposition step oxidation of Al is suppressed and negative ions, including most of the additives in commercial TCP formulations, are repelled from the Al-coated wafer and excluded from the deposited film. A Cr(III)/Zr(IV) oxide film forms on Al during the cathodic step with little contamination by aluminum oxide and other substances. Therefore we simplified the formulation to a Cr(III)/Zr(IV) system with an atomic ratio of Cr:Zr = 3:5. To make solutions of this ratio, 6 g of $KCr(SO_4)_2$ and 8 g of K_2ZrF_6 were first dissolved in 1 L of distilled water, and then diluted to 10 vol % (pH 3.5 ± 0.2) and aged for 24 h before EA deposition.

2.3. Neutron Reflectivity (NR). NR has been extensively used to elucidate interfacial structure in a variety of disciplines but is virtually unknown in corrosion science. The most important advantages of neutron reflectivity for the corrosion research are a greater range of sample environments (e.g., vacuum and aqueous) and quantitative characterization of interfacial properties.

The in situ NR experiments were performed on the Surface Profile Analysis Reflectometer (SPEAR) at the Lujan Neutron Scattering Center, Los Alamos National Laboratory. The incident neutron beam has a broad spectrum of wavelengths, λ, typically from 1.5 to 16 Å. The wavelength of any particular neutron is determined by time-of-flight, because neutrons with different wavelengths have different velocities. This polychromatic character allows a range of scattering vectors, q, to be probed simultaneously at a fixed angle of incidence, θ.

The relationship between λ and q is

$$q = \frac{4\pi \sin\theta}{\lambda} \quad (1)$$

For a NR measurement, q typically extends from 0 to 0.2 Å^{-1}, which is achieved using multiple fixed angles of incidence. A typical NR measurement requires both a low-angle and a high-angle setting. For the in situ NR, however, only low-angle data were measured because we require a rapid measurement with sufficient time resolution to monitor an evolving surface.

The reflected beam from the sample surface is collected by a neutron detector. The ratio of the fluxes of the reflected beam to the incident beam, R, is measured and plotted as a function of q. The data are normalized to one at low q where the beam is 100% reflected. The $R-q$ plot typically shows fringes resulting from the superposition of waves scattered by different layers at the interface between the substrate and environment. The amplitude and attenuation of each wave are determined by the thickness, roughness, and scattering length density (SLD) of the layers. Thickness and roughness represent structural information while the SLD reveals the chemical composition

$$\mathrm{SLD} = \rho \frac{N_A}{M} \sum_{\text{molecule}} b_i \quad (2)$$

where ρ is the mass density; N_A is Avogadro number; M is molecular weight; b_i is the neutron scattering length of atom i; and $\rho(N_A/M)$ is molecular number density. $\Sigma^{b_i}_{\text{molecule}}$ is the sum over neutron scattering lengths of all atoms present in one molecule. The b values are known for all elements.[25]

The analytical tool used for the NR data reduction is Irena[26] 2.35 for Igor Pro 6.10, which inverts the $R-q$ plot (reciprocal space) to the SLD profile (real space). The SLD profile is the SLD as a function of the perpendicular distance from the Si substrate. Since more than one SLD profile may fit the $R-q$ data, physical insight is required to ensure realistic SLD profiles. Fortunately, most parameters in the SLD profile are known, such as the SLD of silica, and the SLD and thickness of Al layer. This information eliminates specious profiles, leaving little freedom in fitting. For the TCP system, we accept only profiles that evolve reasonably under different conditions. Further analysis of these SLD profiles enables us to determine the film composition, the mechanism of TCP passivation, the impact of corrosion on film morphology and the failure mechanism.

2.4. In situ Split Liquid Cell. A key goal of this research was to observe the evolution of the TCP film on anodic sites in AA 2024-T3 when exposed to a chloride-containing aqueous environment. This objective was achieved by building a NR split liquid cell. The split liquid cell isolates the relevant galvanic couple on two separate silicon wafers and allows a reference electrode to be inserted in the liquid cavity between them (Figure 2). The upper wafer is the working electrode, which is interrogated by the neutron beam. The cathodic proton reduction reaction proceeds on the lower wafer, which serves as the counter electrode. A D_2O-based NaCl solution (1 g/100 mL) was injected into the cell. Heavy water (D_2O) is used to minimize incoherent scattering. The cell is made of Macor ceramic (Ceramic Products, Inc., 32 MacArthur Ave, Hasbrouck Heights, NJ), which was also chosen to minimize incoherent scattering.

The working electrode is a 5-mm thick, 75-mm diameter Si wafer coated with a thin layer (<1000 Å) of Al. A similar Au-coated wafer is used for the counter electrode. Under anodic polarization of the working electrode the two wafers mimic the microscopic galvanic couple between the Al matrix and the noble intermetallic inclusions in AA 2024-T3.

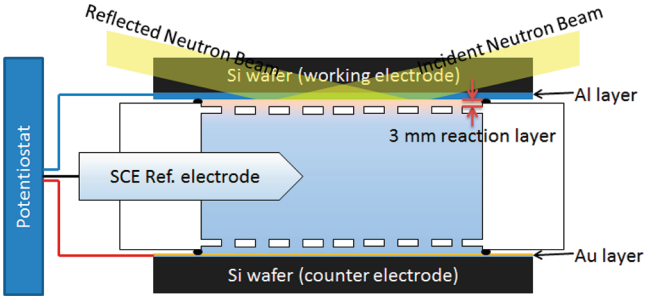

Figure 2. Design of the split liquid cell. The liquid space in the cell is separated into three cavities, a bulk reservoir in middle and two thin reaction layers on both sides. Neutrons penetrate the Si substrate from above and reflect off the film-water interface. The wafer electrodes directly contact the electrolyte in the reaction layer. The thickness of the reaction layer is 3 mm. Holes between the cavities allow NaCl-D_2O solution to flow to the reaction layers to sustain corrosion.

Using the split liquid cell, we performed two in situ corrosion experiments on two different working electrodes: (1) the original Al-coated wafer, which serves as a control; and (2) TCP-coated Al on a Si wafer for the TCP passivity study. The TCP-coated Al working electrode mimics the pitting-prone anodic areas on a TCP treated Al alloy when exposed to a chloride-containing aqueous environment. The TCP morphology and the interface between TCP and Al were investigated by NR under a sequence of potentials starting at the open circuit potential (OCP) and increasing up to the pitting potential where the anodic current rises dramatically.

The D_2O electrolyte is deaerated to ensure that the cathodic process is dominated by the proton reduction reaction. Deaeration also reduces open circuit potential (OCP), leaving a wider passive potential range, which facilitates elucidation of the response of TCP film to varied anodic conditions. Also, in a pitting scenario, the anodic pit is oxygen depleted so deaeration is appropriate.

Using a potentiostat we established an active corrosion environment within the cell, and tracked the applied potential and resulting current during the corrosion process. Meanwhile a neutron beam impinges on the wafer from above and is reflected at the interface between coating surface and electrolyte in the liquid cavity, revealing the evolution of the interface of the TCP film and underlying Al during active corrosion.

3. DATA AND RESULTS

3.1. Electro-assisted (EA) TCP Deposition. The in situ study of TCP film requires a well-defined film, which we achieved using the EA deposition method. Two different cathodic potentials were tested on AA 2024-T3 coupons, −1.50 V vs SCE and −1.25 V vs SCE. During deposition both the applied potential and the current density profiles were recorded as shown in Figure 3.

During initial anodic stage (0−30 s), the current density curves are quite different, but reach the same level (0.35 ± 0.05 mA/cm^2) after 30 s. In cathodic deposition phase, the current density curves are almost identical (30−210 s). For example, all current density curves of the −1.50 V group (red) show a slight decrease from −0.30 ± 0.02 mA/cm^2 to −0.24 ± 0.02 mA/cm^2

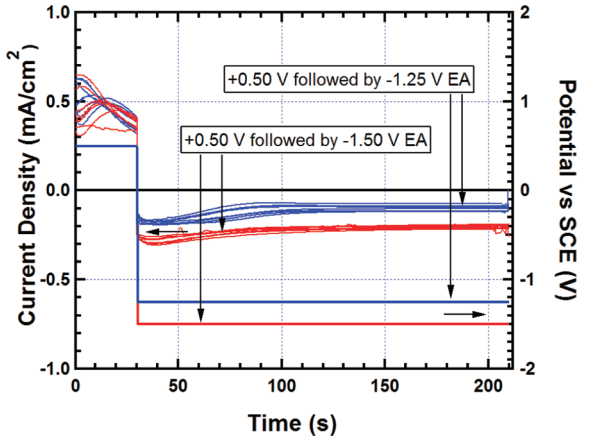

Figure 3. Deposition potential and current density during EA process on AA 2024-T3 coupons: (a) blue, +0.50 V, 30 s followed by −1.25 V, 180 s (straight line); (b) red, +0.50 V, 30 s followed by −1.50 V, 180 s (straight line).

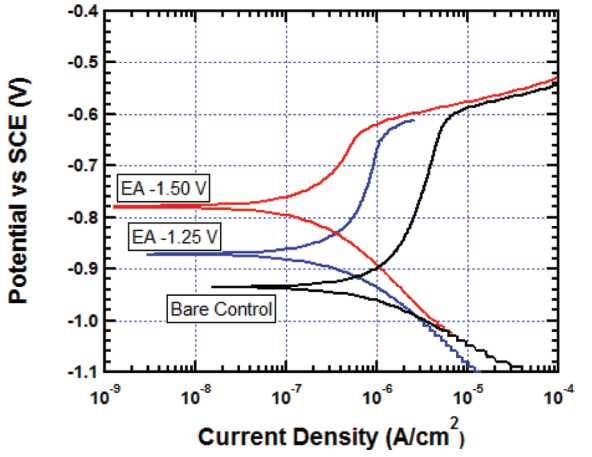

Figure 4. Dynamic DC polarization curves of TCP-treated AA 2024-T3 samples and a bare control in (1 g/100 mL NaCl deaerated aqueous solution). All samples were conditioned at OCP for 30 min prior to the scan. The scan rate was 1 mV/s.

during the time period from 30 to 90 s. After this period, the cathodic current density continues to attenuate slowly (30−90 s), finally reaching at −0.2 ± 0.01 mA/cm^2. Similar behavior was observed for the −1.25 V group with the current stabilizing at −0.1 ± 0.02 mA/cm^2.

After 24 h of room-temperature drying, the TCP-treated AA 2024-T3 and a bare control were compared by dynamic DC polarization (Figure 4). In the presence of the TCP passivation film, the OCP shifted from −950 mV to −770 ± 25 mV (−1.50 V TCP samples) and −870 ± 25 mV (−1.25 V TCP samples), leading to a significant decrease in the anodic current. Compared to the bare control, suppression of the cathodic branch was also observed.

Since the TCP film deposited at −1.50 V performed better than −1.25 V film, so −1.50 V was chosen as a standard for TCP deposition.

3.2. In situ NR of Bare Al. A bare Al-coated wafer was tested first in the split liquid cell. The NR data yielded information on the change in thickness of the Al layer when a constant potential of −930 mV vs SCE was applied, which is an overpotential of +100 mV. This bare-metal study mimicked the pitting area in unprotected AA 2024-T3.

Figure 5 shows the evolution of Al without TCP protection at a constant anodic potential in NaCl-D_2O solution in the split cell. We obtained NR curves (Figure 5a) at the beginning of polarization (blue), and after 3 h of exposure (red). We measured low-angle $R-q$ snapshots at 0−20 min and 180−200 min. The 20 min snapshots provide sufficient time resolution to capture the film thickness change during the active dissolution process.

The 3 h reflectivity curve (red in Figure 5a) flattened after 3-h polarization, indicating a major structural change in the Al coating. Figure 5b gives the SLD profiles, which reveal the change in Al coating thickness. The 0 Å position on abscissa marks the surface of Si wafer. A native SiO_2 layer forms on Si with a thickness of 10−20 Å. Because SiO_2 has a higher SLD than Si, a sharp peak is observed at the wafer surface. The SLD observed at large distances from the surface is the value expected for the NaCl-D_2O environment (6.37×10^{-6} Å^{-2}). The region between SiO_2 peak and NaCl-D_2O environment is the Al layer with a constant SLD of 2.14×10^{-6} Å^{-2}. Comparing the SLD profiles before (blue curve) and after 3 h polarization (red curve), the thickness of Al changes from 860 ± 10 Å to 500 ± 10 Å.

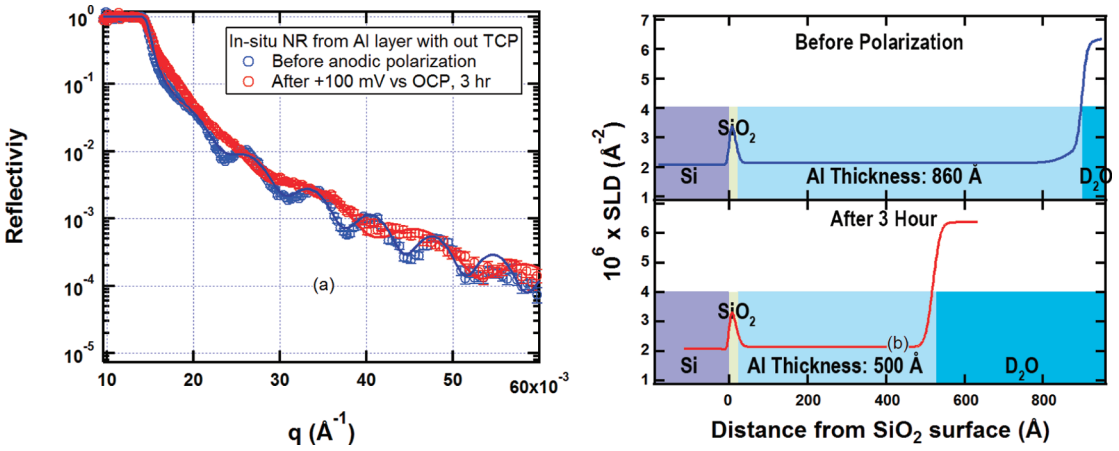

Figure 5. (a) SPEAR NR data ($R-q$ plots) on a corroding Al layer in a split liquid cell. The data before and after 3 h exposure at 100 mV noble to the OCP in deaerated NaCl-D_2O solution show that the q spacing between fringes expands, indicating reduced thickness of Al layer. (b) SLD profiles based on the $R-q$ plots. The Al layer thickness changed by ∼360 Å (from ∼860 Å before exposure to ∼500 Å after 3 h of exposure). A color scheme is adopted in the SLD profile to highlight the different layers present.

The bare Al-coated wafer mimics the unprotected anodic sites on AA 2024-T3 when exposed to a corrosive environment. Also this experiment shows that the corrosion rate is matched to the time-resolution of the NR instrument. Below we show consistency between Al dissolution measured by NR and by the measured anodic current.

3.3. In situ NR Study of TCP Passivity. To quantify TCP protection of the pitting-prone anodic sites in the alloy, we observed the evolution of the TCP-covered Al anode exposed to progressively increasing anodic potentials in NaCl-D_2O solution. The DC polarization data in the split liquid cell were measured prior to the in situ NR in order to find the OCP (Figure 6). A sequence of NR snapshots revealed the TCP structure at different potentials above the OCP, which occurs at -1.00×10^3 mV. Each potential was applied for 1 h. Each low-angle snapshot took 20 min, which is suitable for observation of film evolution.

Figure 7a shows a sequence of $R-q$ plots from the TCP-coated sample at different potentials. No significant change was observed during the first 12 h when potential was below −800 mV (red curves), indicating passivity. When the potential was nobler than the pitting potential ($E_{pit} \approx -800$ mV), however, the TCP film started to degrade (Figure 7a, blue). Eventually the TCP film and entire Al layer dissolved as revealed by the disappearance of NR fringes (Figure 7a, black).

The structural change in the TCP passive films under anodic conditions is revealed by the SLD profiles in the passive state (Figure 7b, red), and after the film disrupted (Figure 7b, black). The red SLD profile in Figure 7b shows a stable TCP film between ~150 and ~760 Å. Below 150 Å is the Al layer, whose thickness decreased from ~400 to ~150 Å due to the anodic step of EA-TCP deposition process. When the applied potential is more noble than −800 mV, however, both the TCP layer and the Al layer disappear (black profile), leaving wafer substrate directly exposed to D_2O solution (marked by the sharp SLD drop at 0 Å).

These experiments reveal that TCP has a dramatic effect on anodic polarization of Al. The bare metal film uniformly degrades over several hours under slight anodic polarization. With TCP protection, however, the Al layer is completely stable to an overpotential of +200 mV, after which Al starts to oxidize.

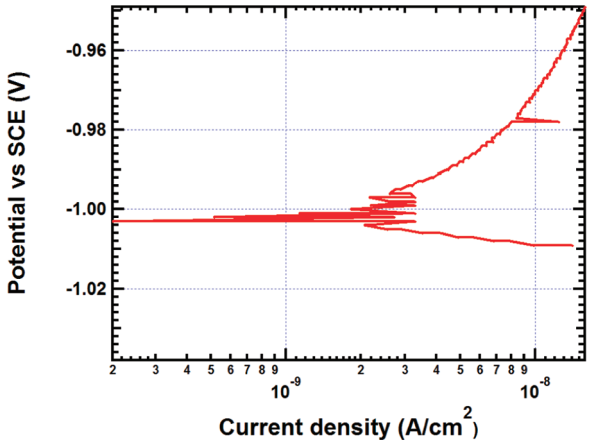

Figure 6. Dynamic DC polarization curves from TCP-treated Al-coated wafer anode in the split liquid cell. The liquid cell was filled with NaCl-D_2O solution and stabilized for 30 min prior the measurement. The OCP is indicated at -1.00×10^3 mV.

4. DISCUSSION

The in situ NR data and corresponding electrochemical records harbor insights into the protection and failure of TCP-coated Al. Here we discuss:

1 the difference in the corrosion rate of the bare and TCP-protected Al anode based on NR and electrochemical data;
2 the passive TCP structure in a pitting scenario;
3 the penetration of aqueous phase into the passive TCP film under a sequence of potentials;
4 the failure mode when the applied potential compromises TCP protection.

First of all, the in situ 3 h polarization on the bare Al layer at an overpotential of +100 mV validates the correlation between the in situ electrochemical data and simultaneous NR SLD profiles (Figure 5). The current density collected indicates dissolution of the Al layer (Figure 8). Assuming the anodic current is due to Al oxidation, the dissolved Al per unit area can be calculated based

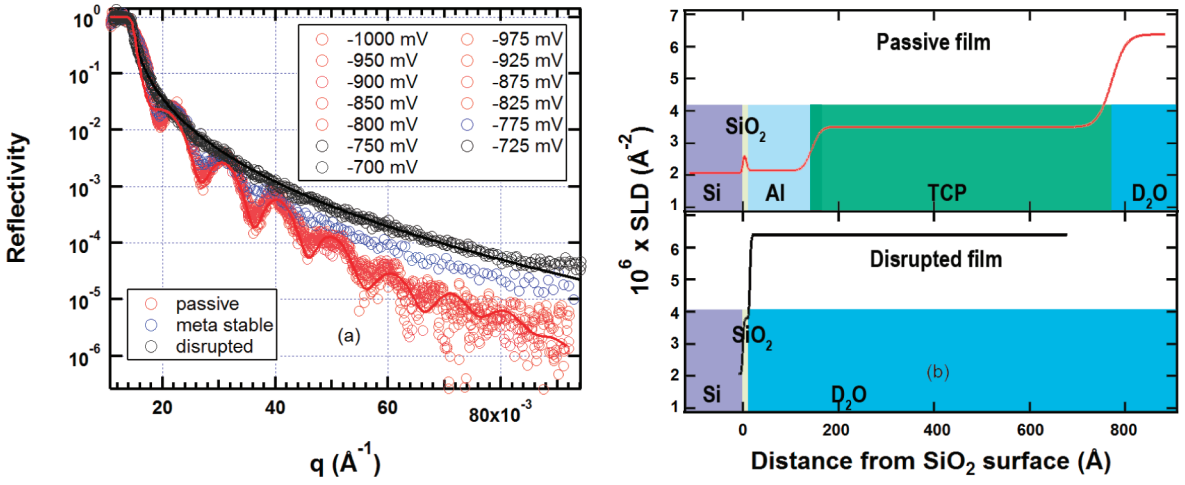

Figure 7. (a) SPEAR NR data ($R-q$ plots) for in situ TCP under anodic potentials. Below −800 mV, the film is stable. However, fringes disappeared after the potential reached −750 mV, indicating the TCP coating and Al layer were stripped. (b) SLD profiles based on $R-q$ plots show the disappearance of TCP film as well as the Al layer after the potential exceeded E_{pit}. The position of D_2O solution drops from ~760 to 0 Å.

on integration of the measured current density between 0 and 180 min according to Faraday's Law.

$$FZ\frac{V\rho_{Al}}{AM_{Al}} = \int_0^{180\ \mathrm{min}} i(t)\mathrm{d}t = 14\,600\ \mu\mathrm{C} \qquad (3)$$

where F is the Faraday constant (96,485 C/mol); Z is the valence of Al^{3+}; V is the volume of dissolved Al; A in is total area of the corroding surface; ρ_{Al} is the mass density of Al; M_{Al} is the atomic weight of Al, i is the current density; and t is time. The dissolved Al in units of volume per unit area, V/A, is calculated to be 380 ± 20 Å.

On the basis of the measured current density, the native oxide layer showed little resistance against anodic attack. The NR SLD profiles indicate the same behavior. Two NR in situ snapshots on the anode (Figure 5) were taken at 0−20 min and 180−200 min. The SLD profiles give an Al thickness change of 360 ± 10 Å, consistent with the thickness change based on the integration of the recorded current density in Figure 8. Consistency also assures that the electrochemistry is not compromised by the design of the split cell.

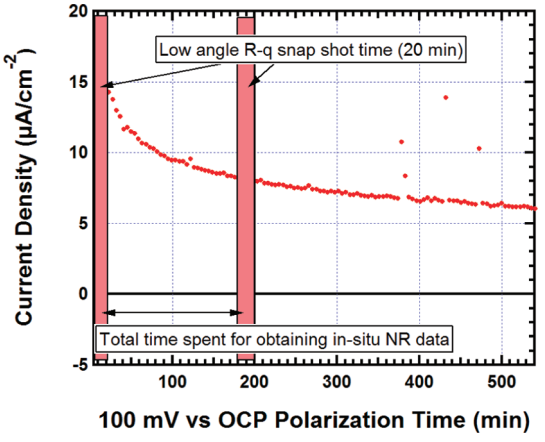

Figure 8. Current density recorded for bare Al in the split cell. The reduction in Al layer thickness is in agreement with the average in current density. The durations of the NR snapshots are marked as vertical bars. The current density was measured during the 3 h polarization experiment.

The evolution of current density for the TCP-protected sample shows radically different behavior compared to the bare Al. The protected system shows significant passive character even when applied the potential is +200 mV noble to the OCP.

The measured current density curves corresponding to each applied anodic potential are plotted in Figure 9a (−975 to −800 mV) and Figure 9b (−975 to −725 mV). In Figure 9a, the measured current density remained below 10 nA/cm^2 at each polarization step. The TCP film effectively protects the underlying Al layer, indicating a passive state. The current density curve at −800 mV (red), however, showed some peculiarities. Large "noise" peaks continuously popped up during the 1 h step. Although the average current declined, these peaks imply some local breakdown in the TCP film that is immediately repassivated. The cause of repassivation is not clear. Perhaps Al corrosion product blocks the newly formed ion channels in TCP film. The current density curves for subsequent steps (−775, −750, and −725 mV) are included in Figure 9b. The current at −775 mV rapidly increased from nA/cm^2 to μA/cm^2. The TCP film loses its passivity at this potential and Al layer starts to dissolve. At −750 and −725 mV dissolution continues until there is no Al left on the silicon wafer.

The passive film structure and failure mechanism in a pitting scenario are revealed by analysis of the NR data in Figure 7 for TCP-protected Al-wafer. When in the passive range (below −800 mV), the TCP film is stable as indicated by the identical red $R-q$ plots in Figure 7a and SLD profile in Figure 7b. The thickness of the Al layer did not change during these steps. Above the −800 mV, TCP no longer suppresses the dissolution of Al layer. The entire system (Al and TCP) strips, leaving the oxide-covered silicon substrate directly in contact with the D_2O electrolyte (Figure 7b). The metastable state (−775 mV) will be discussed later after we examine the water content of the TCP layer in the passive state.

To quantify the D_2O penetration into in the passive TCP film, we compared the SLD profile of the TCP film before and after D_2O exposure (Figure 10) below −800 mV. The SLD profile of the dry sample shows that a thin, dense interfacial layer exists between the metal and the bulk TCP film. In the wet state, this

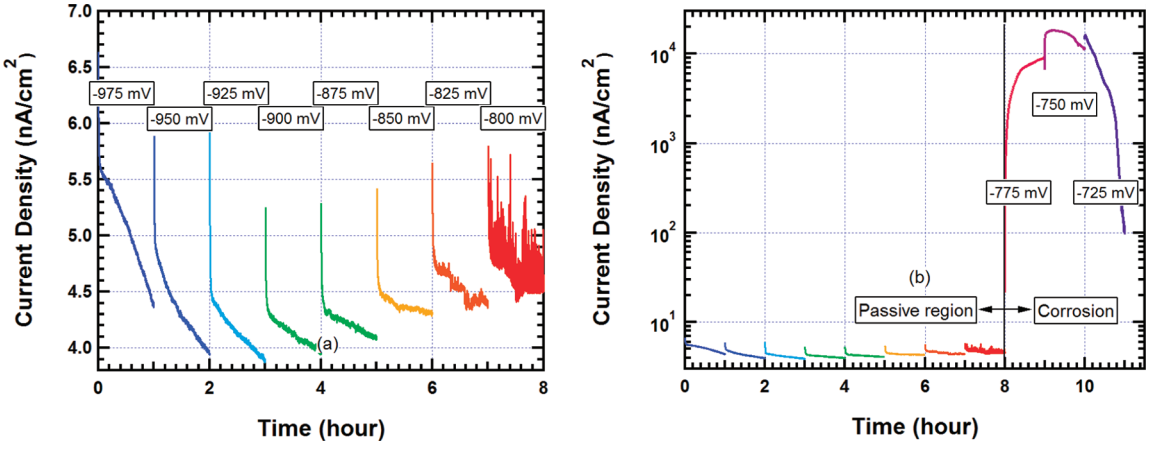

Figure 9. Current density curves of a TCP-coated sample after each potential step. (a) Recorded current densities in the passive region (−975 to −800 mV vs SCE) were under 10 nA/cm^2. The red curve (at −800 mV) showed some instability, as indicated by the noise peaks. (b) The current density for potentials more noble than −775 mV jumped to μA/cm^2 scale, but eventually dropped back after the Al dissolved, leaving a bare silicon wafer. The curve at −725 mV illustrates this behavior within the time window of the experiment.

layer is masked in the high *SLD* wet film. We determined the composition of the bulk film in the dry state previously by a combination of neutron reflectivity and X-ray reflectivity: $Cr_2O_3 \cdot iH_2O \cdot x(ZrO_2 \cdot jH_2O)$ (i = 2.10 ± 0.55, j = 1.60 ± 0.45, and x = 0.85 ± 0.14).[15]

Comparing the SLD profiles of TCP films in the room-temperature dried state (Figure 10, blue curve), and in the split liquid cell (Figure 10, red curve), the *SLD* of the TCP film increases from $1.98 \pm 0.06 \times 10^{-6}$ Å^{-2} to $3.6 \pm 0.1 \times 10^{-6}$ Å^{-2}, while the thickness does not change significantly. The SLD increase can be explained by exchange of D_2O for the H_2O in Cr and Zr oxide hydrates that constitute the TCP film.

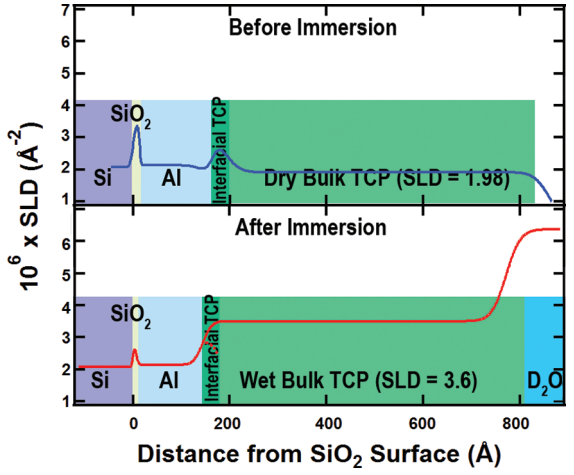

Figure 10. SLD profiles of RT-dried TCP samples before polarization (blue curve).[15] A dense interfacial TCP layer is observed between the bulk TCP film and Al. The SLD profile after exposure (red curve, from Figure 7b) is plotted for comparison. The dense interfacial layer still exists in the wet state but is overwhelmed by the bulk TCP layer, which has higher SLD.

The molecular fraction, f, converted from hydrate to deuterated is calculated as

$$\frac{3.6 \times 10^{-6}\text{Å}^{-2}}{1.98 \times 10^{-6}\text{Å}^{-2}} = \frac{b_{Cr2O3 \cdot xZrO2 \cdot (i+xj)((1-f)H2O+fD2O)}}{b_{Cr2O3 \cdot xZrO2 \cdot (i+xj)H2O}} \quad (4)$$

where i = 2.10 ± 0.55, j = 1.60 ± 0.45 and x = 0.85 ± 0.14.[15]

Given the neutron scattering lengths of the relevant compounds

$$b_{Cr2O3} = 2.46 \times 10^{-4}\text{Å}$$

$$b_{ZrO2} = 1.876 \times 10^{-4}\text{Å}$$

$$b_{H2O} = -0.167 \times 10^{-4}\text{Å}$$

$$b_{D2O} = 1.915 \times 10^{-4}\text{Å}$$

Equation 4 yields f = 40 ± 5%, which means 40% of H_2O molecules in the Cr(III)/Zr(IV) oxide hydrate is exchanged, whereas the TCP film remains protective. This result shows that the bulk TCP film is not chemically inert when exposed to an aqueous environment, although it remains passive. Water molecules from the salt solution penetrate the bulk TCP layer by replacing the original water of hydration.

TCP passivity is attributed to the suppression of NaCl-D_2O solution penetration, hence acting as barrier against ion transport. Since the TCP bulk film retains its original dry-state structure with no swelling, the Cr_2O_3/ZrO_2 matrix is not altered by exchange of hydrate water. If bulk salt solution penetrated the film it would swell. In the absence of such swelling, transport of Na^+, Cl^-, and Al^{3+} is suppressed, as there is no bulk water to stabilize these ions. Suppression of ionic transport precludes Al dissolution. In addition, the dense interfacial layer is immune to both deuterate-hydrate exchange and bulk water penetration, so this layer also blocks ion transport.

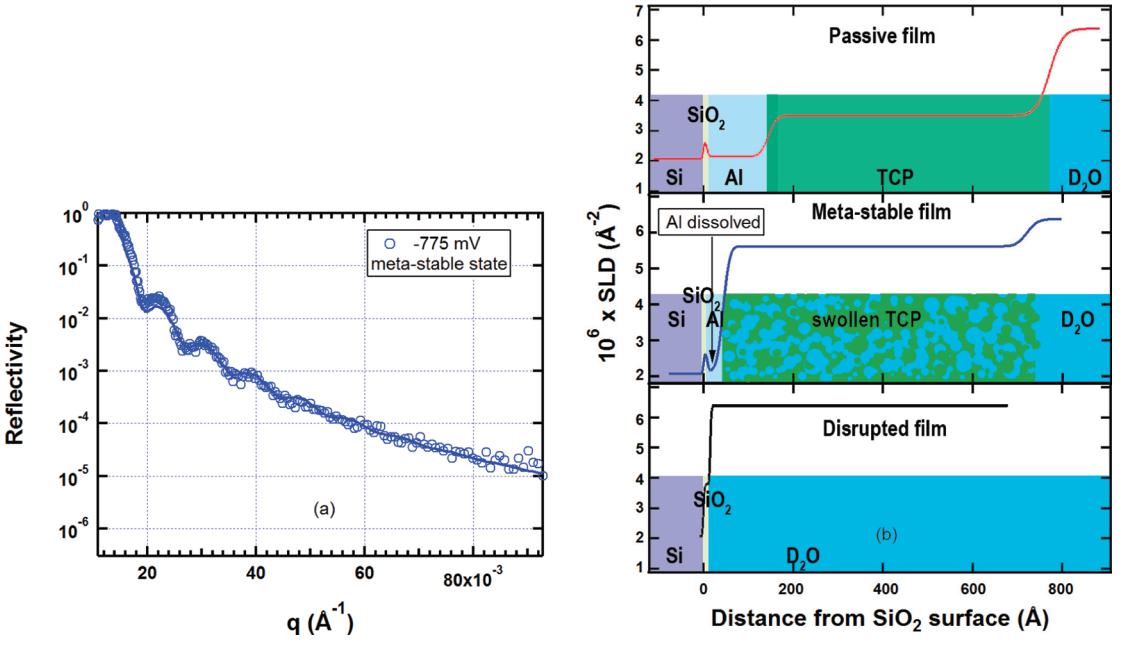

Figure 11. (a) NR data (R–q plots) for the metastable state at −775 mV. (b) SLD profiles of the metastable state compared to the passive and failed states. In the metastable state the Al layer dissolves and TCP film swells. The SLD of the TCP layer is $5.7 \pm 0.1 \times 10^{-6}$ Å^{-2} and the thickness is 690 ± 20 Å.

dx.doi.org/10.1021/am200845v |*ACS Appl. Mater. Interfaces* 2011, 3, 4206–4214

Failure of the TCP film is attributed to penetration of bulk salt solution, which facilitates ion transport. Evidence for this failure mechanism comes from examination of the NR data in the metastable state at −775 mV. According electrochemical data (Figure 9) the TCP film loses protective character at this potential.

The $R - q$ plot in the metastable state is shown in Figure 11a. Figure 11b compares the SLD profiles in the passive, metastable and failed states. In the metastable state the Al layer thins while the TCP film swells significantly, as indicated by both increased thickness and higher SLD. Compared to passive state the SLD increases from $3.6 \pm 0.1 \times 10^{-6}$ Å^{-2} to $5.7 \pm 0.1 \times 10^{-6}$ Å^{-2}. The higher SLD can be explained by complete conversion of crystal hydrate water plus physical invasion of bulk salt solution.

Given the SLD of D_2O (6.37×10^{-6} Å^{-2}), and $SLD_{swollenTCP}$ (5.7×10^{-6} Å^{-2}), the volume fraction, ϕ, occupied by NaCl-D_2O bulk solution in the metastable film can be estimated if we assume complete exchange of crystal hydration water plus penetration of bulk D_2O

$$\mathrm{SLD_{swollenTCP}} = (1-\phi)\mathrm{SLD_{(Cr2O3 \cdot iD2O \cdot x(ZrO2 \cdot jD2O))}} + \phi \mathrm{SLD_{D2O}} \quad (5)$$

where $\mathrm{SLD_{Cr2O3 \cdot iD2O \cdot x(ZrO2 \cdot jD2O)}}$ can be calculated from the known scattering lengths.

$$\frac{\mathrm{SLD_{Cr2O3 \cdot iD2O \cdot x(ZrO2 \cdot jD2O)}}}{\mathrm{SLD_{Cr2O3 \cdot iH2O \cdot x(ZrO2 \cdot jH2O)}}} = \frac{b_{\mathrm{Cr2O3 \cdot iD2O \cdot x(ZrO2 \cdot jD2O)}}}{b_{\mathrm{Cr2O3 \cdot iH2O \cdot x(ZrO2 \cdot jH2O)}}} \quad (6)$$

Substitution yields:

$$\phi = \frac{5.7 \times 10^{-6}\text{Å}^{-2} - 4.84 \times 10^{-6}\text{Å}^{-2}}{6.37 \times 10^{-6}\text{Å}^{-2} - 4.84 \times 10^{-6}\text{Å}^{-2}} = 50 \pm 10 \text{ vol \%} \quad (7)$$

The chloride-containing aqueous phase occupies approximately 50 vol % of the swollen TCP film. Both bulk and interfacial TCP layers are penetrated by salt solution. The aqueous environment now directly contacts the Al. Both Cl^- and Al^{3+} ions diffuse through the film. The entire passivation system fails and Al oxidizes as indicated by the recorded current density curves (Figure 9b).

5. CONCLUSIONS

The techniques developed here give corrosion researchers their first quantitative look at the composition and physical structure of passive films in an active corrosion environment. These NR data reveal the corrosion process of bare and TCP-coated Al and, for the first time, the structure and morphology of TCP film in aqueous solution under pitting conditions.

The in situ experiment on bare Al anode, first of all, verifies the correlation of NR SLD profiles with the electrochemical response. In chloride-containing aqueous environment, a uniform Faradaic corrosion process was observed near the OCP on a bare Al surface as supported by the recorded corrosion current density and thickness change in the Al layer measured by NR.

Second, a stable TCP film is observed by NR when the film remains protective in a chloride-containing aqueous environment. Neither the TCP film nor the underlying Al show any change when the applied anodic potential increases from OCP to +200 mV vs OCP over a 12 h period. This passive character is proven by both current density, which remains in the nA/cm^2 range, and NR data, which show identical $R-q$ plots and SLD profiles.

Third, based on SLD profiles of the TCP film under stable conditions, approximately 40% of the solid hydrate water in the bulk TCP layer is exchangeable when exposed to an aqueous environment. In spite of exchange of hydration water, however, the Cr_2O_3/ZrO_2 matrix retains its original dry-state structure with no swelling. In the absence of bulk solution in the film, transport of Na^+, Cl^- and Al^{3+} is suppressed and the underlying aluminum remains fully protected. Passivity is attributed to suppression of ion transport by both the bulk and interfacial layers.

Finally, when the potential reaches pitting potential, the TCP film swells and looses passivity. The underlying aluminum dissolves as indicated by the current density in μA/cm^2 scale. The TCP film swells, but does not completely dissolve. In this swollen state, the chloride-containing aqueous phase penetrates the entire TCP film including the dense layer at the metal interface. Ion transport is no longer suppressed so the aluminum under the swollen TCP film oxidizes. The TCP film itself disappears with a 25 mV increase in applied potential.

AUTHOR INFORMATION

Corresponding Author

*E-mail: dale.schaefer@uc.edu. Tel: +1 513 556 5431. Fax: +1 206 600 3191.

ACKNOWLEDGMENT

This research is funded by a seed contract from the Strategic Environmental Research and Development Program. Neutron reflectivity measurements were performed at the Lujan Neutron Scattering Center (LANSCE) at Los Alamos National Laboratory (LANL) under support by LANL under DOE Contract W7405-ENG-36, and by the DOE office of Basic Energy Sciences. We benefited from discussions with Craig Matzdorf on formulation of TCP coatings. We thank Hillary Smith, Jaroslaw Majewski, and Michael Jablin for their assistance in collecting the reflectivity data. We thank Mr. Douglas Hurd for help fabricating the split cell and cell accessories.

REFERENCES

(1) Yasakau, K. A.; Zheludkevich, M. L.; Lamaka, S. V.; Ferreira, M. G. S. *J. Phys. Chem. B* **2006**, *110* (11), 5515–5528.

(2) Buchheit, R. G.; Grant, R. P.; Hlava, P. F.; Mckenzie, B.; Zender, G. L. *J. Electrochem. Soc.* **1997**, *144* (8), 2621–2628.

(3) Apte, A. D.; Tare, V.; Bose, P. *J. Hazard. Mater.* **2006**, *128* (2−3), 164–174.

(4) Berger, R.; Bexell, U.; Grehk, T. M.; Hornstrom, S. E. *Surf. Coat. Technol.* **2007**, *202* (2), 391–397.

(5) Bishop, C. V.; Wynn, P. C. *Trans. Inst. Met. Finish* **2001**, *79*, B34–B34.

(6) Buchheit, R. G.; Guan, H.; Mahajanam, S.; Wong, F. *Prog. Org. Coat.* **2003**, *47* (3−4), 174–182.

(7) Kendig, M. W.; Buchheit, R. G. *Corrosion* **2003**, *59* (5), 379–400.

(8) Kolics, A.; Besing, A. S.; Wieckowski, A. *J. Electrochem. Soc.* **2001**, *148* (8), B322–B331.

(9) *Non-Chromate Aluminum Pretreatments Phase I Report*; Environmental Security Technology Certification Program: Arlington, VA, 2003.

(10) *Non-Chromate Aluminum Pretreatments Phase II Report*; Environmental Security Technology Certification Program: Arlington, VA, 2004.

(11) Li, L.; Swain, G. P.; Howell, A.; Woodbury, D.; Swain, G. M. *J. Electrochem. Soc.* **2011**, *158* (9), C274–C283.
(12) Hurley, B. L.; McCreery, R. L. *J. Electrochem. Soc.* **2003**, *150* (8), B367–B373.
(13) Dardona, S.; Jaworowski, M. *Appl. Phys. Lett.* **2010**, *97* (18).
(14) Matzdorf, C.; Kane, M.; Green, J. U.S. Patent Appl. 09/702,225, Patent No. U.S. 6 375 726 B1, Apr 23, 2002.
(15) Dong, X.; Wang, P.; Argekar, S.; Schaefer, D. W. *Langmuir* **2010**, *26* (13), 10833–10841.
(16) Wang, P.; Dong, X.; Schaefer, D. W. *Corros. Sci.* **2010**, *52* (3), 943–949.
(17) Wang, P.; Schaefer, D. W. *Langmuir* **2009**, *26* (1), 234–240.
(18) Kern, W. *Handbook of semiconductor wafer cleaning technology science, technology, and applications*; Kern, W., Eds.; Noyes Publications: Park Ridge, NJ, 1993; p 121.
(19) Campestrini, P.; van Westing, E. P. M.; Hovestad, A.; de Wit, J. H. W. *Electrochim. Acta* **2002**, *47* (7), 1097–1113.
(20) Hughes, A. E.; Taylor, R. J.; Hinton, B. R. W. *Surf. Interface Anal.* **1997**, *25* (4), 223–234.
(21) Kulinich, S. A.; Akhtar, A. S.; Susac, D.; Wong, P. C.; Wong, K. C.; Mitchell, K. A. R. *Appl. Surf. Sci.* **2007**, *253* (6), 3144–3153.
(22) McGovern, W. R.; Schmutz, P.; Buchheit, R. G.; McCreery, R. L. *J. Electrochem. Soc.* **2000**, *147* (12), 4494–4501.
(23) Vasquez, M. J.; Halada, G. P.; Clayton, C. R.; Longtin, J. P. *Surf. Interface Anal.* **2002**, *33* (7), 607–616.
(24) Xia, L.; McCreery, R. L. *J. Electrochem. Soc.* **1999**, *146* (10), 3696–3701.
(25) Roe, R. J. *Methods of X-ray and Neutron Scattering in Polymer Science*; Mark, J. E., Roe, R. J., Eds.; Oxford University Press: New York, 2000; p 21.
(26) Ilavsky, J.; Jemian, P. R. *J. Appl. Crystallogr.* **2009**, *42*, 347–353.